

## Phase-field simulation of stripe arrays on metal bcc(110) surfaces

Yan-Mei Yu,<sup>1,2,3</sup> Rainer Backofen,<sup>1</sup> and Axel Voigt<sup>1</sup>

<sup>1</sup>*Institut für Wissenschaftliches Rechnen, Technische Universität Dresden, 01062 Dresden, Germany*

<sup>2</sup>*Institute of Physics, Chinese Academy of Science, P. O. Box 603, 100190 Beijing, China*

<sup>3</sup>*Beijing National Laboratory for Condensed Matter Physics, Beijing 100190, China*

(Received 1 February 2008; published 22 May 2008)

By using a phase-field model, we simulate formation and growth of stripe arrays starting with anisotropic growth of islands under the Ehrlich-Schwoebel barrier on metal bcc(110) surfaces. The anisotropy is incorporated in terms of attachment kinetics that is locally limited at the island edge aligned to the  $y$  axis (or  $\langle 100 \rangle$ ) and instantaneous at the island edge aligned to the  $x$  axis (or  $\langle 110 \rangle$ ). By reproducing the stripe arrays under various anisotropy magnitudes, we investigate dynamics of formation and growth of the stripe arrays. While enhancing coarsening in the  $y$  direction, the anisotropy suppresses coarsening in the  $x$  direction at the early stage, which contributes to formation of stripe arrays. At long times, the stripe arrays develop the quasiperiodic uniaxial structure with the selected transversal slope and the decreasing longitudinal slope as consequence of competition between coarsening and roughening. At the case of the large anisotropy magnitude, the fast roughening is caused by the strongly limited attachment kinetics, where the transversal coarsening turns fast and then the uniaxial growth is broken finally. For the weak roughening at the case of the reduced anisotropy magnitude, the slow transversal coarsening is achieved with the fast longitudinal coarsening, which contributes to the stripe arrays of the regular period and the increasing uniaxial length. Such arrays have the potential to be used as templates to grow one-dimensional nanostructures.

DOI: [10.1103/PhysRevE.77.051605](https://doi.org/10.1103/PhysRevE.77.051605)

PACS number(s): 81.15.Aa, 68.35.Fx, 68.35.Ct

### I. INTRODUCTION

The epitaxial growth on metal surfaces often manifests striking self-assembled nanostructures. On metal (100) and (111) surfaces pyramids and mounds have been well evidenced by numerous experiments and simulations [1–3]. Due to the Ehrlich-Schwoebel (ES) energy barrier that inhibits downward transportation of adatoms at step edges, the island nucleation becomes easy on top atomic-layers, which causes multilayered stacks of two-dimensional (2D) islands that resemble the pyramids and mounds [4–7]. Likewise, multilayered structures of islands are caused by the ES barrier on metal (110) surfaces. However, the multilayered structures represent the strong anisotropy on the metal (110) surfaces. The anisotropic growth contributes to low-symmetric nanostructures that are different from the pyramids and mounds [8,9].

Being the prototype of the low-symmetric multilayered structures of the islands on metal bcc (110) surfaces, stripe arrays of Fe and W have been reported by recent experiments [10–14]. These stripes consist of a periodic uniaxial structure. If used as the template, this structure provides a promising bottom-up fabrication approach of the one-dimensional nanostructure [13,14]. Controlling the stripe growth of uniform periodicity is necessary for the potential technical applications, which demands understanding of the stripe growth mechanism on the metal bcc (110) surfaces. In a few past works, a KMC simulation [11] verified growth of elongated mounds on Fe (110) surfaces at the early stage. There is still much less known about the growth of the stripe arrays at the large scale.

In this paper, we simulate the growth dynamics of the stripe arrays on the metal bcc (110) surfaces by using a phase-field model. The anisotropy of the metal bcc (110)

surfaces is incorporated by formulating the orientation-dependent atomic attachment kinetics at the island edges. Our simulations reproduce the experimentally observed stripe arrays qualitatively [13,14]. The dynamics of formation and growth of the stripe arrays is investigated. Due to the anisotropy, the island coarsening is slow in the  $x$  direction and fast in the  $y$  direction, which causes formation of stripe arrays at the early stage. At long time, the stripe arrays develop the quasiperiodic uniaxial structure as a consequence of competition between coarsening and roughening for the selected transversal slope and the decreasing longitudinal slope. In the case of large anisotropy magnitude, the strongly limited attachment kinetics causes fast roughening as well as fast transversal coarsening, which finally breaks the uniaxial growth. In the case of reduced anisotropy magnitude, the fast longitudinal coarsening is achieved with the roughening and transversal coarsening being slow, which contributes to the stripe arrays of the regular period and the increasing uniaxial length.

The remaining part of this paper is organized as follows. In the next section we describe our phase-field model and parameters for the island growth of the anisotropic atomic attachment kinetics. In Sec. III we present our simulated results. In Sec. IV we discuss formation and growth dynamics of the stripe arrays with regard to the anisotropic attachment kinetics. Finally we present our conclusion in Sec. V.

### II. PHASE-FIELD MODEL

Allowing for simulation of epitaxial growth at large scales with the key atomic kinetics included, the phase-field method has been adapted to treat step-flow growth of thin films and epitaxial growth of isotropic mounding islands [15–20]. Here, we use a layer-by-layer model of the island growth

[20,21]. For the multilayered structure, we choose the height direction of the island as the  $z$  direction and take the intratomic layer (AL) as the  $xy$  plane. We use a phase-field variable  $\phi(x,y)$  to describe ALs of different heights. The values of  $\phi$  being  $1, 2, 3, \dots, n$  correspond to the first, second, third,  $\dots, n$ th AL from the starting surface, respectively. The sharp step between the different ALs is described by the spatial transition zone (STZ) of  $\phi$ , which can be identified by  $\nabla\phi \neq 0$ .

The phase-field equation is formulated as follows:

$$\frac{\partial\phi}{\partial t} = \frac{1}{\tau} [\nabla \cdot (W^2 \nabla \phi) - 2 \sin 2\pi\phi - 2\lambda(\cos 2\pi\phi - 1)u] + \lambda_n u^{i+1}, \quad (1)$$

where  $W$ ,  $\tau$ , and  $\lambda$  are the phase-field model parameters, and  $u$  is the local adatom density. On the right-hand side of Eq. (1), the first term describes the step aggregation according to the time derivation of the effective Hamiltonian of the step growth [15,16,21]. We add the second term to describe the island nucleation. As formulated in the rate equation [22],  $i$  is the critical size of the island nucleation and  $\lambda_n$  is the parameter of the nucleation kinetics.

The local variable  $u$  obeys the following equation:

$$\frac{\partial u}{\partial t} = \nabla \cdot (D \nabla u) - \frac{\partial\phi}{\partial t} + \Omega \delta(\vec{r} - \vec{r}') \delta(t - t'), \quad (2)$$

where the first term on the right-hand side describes the surface diffusion, herein  $D$  is the diffusion coefficient of adatoms. The second term formulates the depletion of adatoms for the island growth. The third term describes the deposition, which adds new adatoms at the point  $\vec{r}'$  randomly every time interval that is determined by  $F$ , wherein  $F$  is the actual deposition flux of the adatoms.

In the thin-interface analysis [23], the phase-field parameter is determined as the following equations:

$$d_0 = a_1 \frac{W}{\lambda}, \quad (3)$$

$$\beta = \frac{a_1}{\lambda} \frac{\tau}{W} \left[ 1 - a_2 \lambda \frac{W^2}{D\tau} \right], \quad (4)$$

where  $d_0$  describes deviation of the local equilibrium concentration at a curved step from that at a straight step according to  $d_0 = \Omega c_{\text{eq}} \gamma / k_B T$ , herein  $\Omega$  is the lattice area,  $c_{\text{eq}}$  is the equilibrium adatom density along the straight step,  $\gamma$  is the isotropic step stiffness,  $k_B$  is the Boltzmann constant, and  $T$  is the temperature. The parameter  $\beta$  reflects the interface kinetics in terms of  $\beta \sim 1/\mu$ , wherein  $\mu$  is the attachment kinetics coefficient of the adatom at the island edge. The constants  $a_1 = 0.36$  and  $a_2 = 0.51$  are set in the thin-interface analysis. In the limit of the instantaneous attachment kinetics with  $\mu \rightarrow \infty$  and  $\beta = 0$ , Eq. (4) reduces to  $\tau_0 = a_1 a_2 W^3 / d_0 D$ .

First, we write  $D$  as  $D(\phi)$  so as to imitate the up-down asymmetry of the adatom motion on the island boundary induced by the ES barrier. Outside of the STZ,  $D(\phi)$  is formulated as  $D_0 = \Omega v \exp[-E_d / k_B T]$  with the diffusion barrier  $E_d$ . In the STZ region of the positive  $\nabla^2\phi$ , which corre-

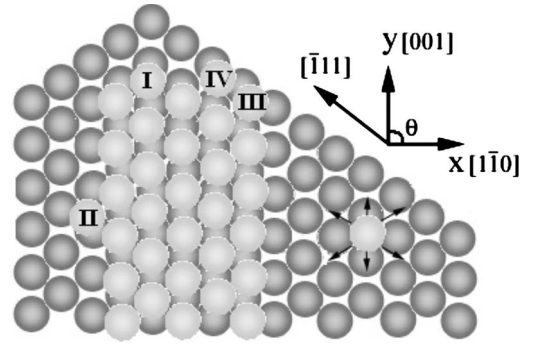


FIG. 1. The lattice model of the anisotropy on the bcc (110) surface. Attachment of atom I at the  $\langle 110 \rangle$  edge is easy, while attachment of atom II at the  $\langle 001 \rangle$  edge is difficult. The easy diffusion along the  $\langle 111 \rangle$  orientation helps atom III stay at the  $\langle 111 \rangle$  edge, which further allows for atom IV attaching at the  $\langle 110 \rangle$  edge.

sponds to the upward step,  $D(\phi)$  is reduced gradually to zero (that is substituted by a nonzero value being far less than  $D_0$  in the computation code) in order to imitate the inhibited terrace-climbing motion of the adatom. In the STZ region of the negative  $\nabla^2\phi$ , which corresponds to the downward step, we formulate  $D(\phi) = D_0 \exp(-E_s / k_B T)$  to imitate the suppression of the ES barrier  $E_s$  on the downward motion of the adatom.

Further, we formulate  $\tau(\theta)$  to imitate the anisotropy, wherein  $\theta$  is the angle between the normal to the island boundary to the  $x$  direction. The anisotropy is determined according to the geometry of the metal bcc (110) surface. As shown in Fig. 1, the step with the edge along  $\langle 110 \rangle$  is openly packed, which provides the advantageous site for the adatom (denoted by “atom I”) to attach. In contrast, the step with the edge along  $\langle 100 \rangle$  is closely packed, where attachment of the adatom (denoted by “atom II”) is difficult. Therefore the atomic attaching probability is high locally at the step segment aligned to  $\langle 110 \rangle$  and low at the step segment aligned to  $\langle 100 \rangle$  [10]. The geometry of the metal bcc (110) surface also causes the diffusive anisotropy that the adatom migrates easily along  $\langle 111 \rangle$ , but difficultly along  $\langle 001 \rangle$  [11,12]. On the terrace the effect of anisotropic diffusion is not certain, if the diffusion along  $\langle 001 \rangle$  is realized by the combined  $\langle 111 \rangle$  diffusion in the curved pathway. However, at the island edge the diffusion anisotropy supports the anisotropic attachment kinetics. Easy diffusion along  $\langle 111 \rangle$  helps the adatom (denoted by “atom III”) stay at the  $\langle 111 \rangle$  edge and helps the adatom (denoted by “atom IV”) stick at the  $\langle 110 \rangle$  edge, whereas the difficult diffusion along  $\langle 001 \rangle$  keeps atom II off the  $\langle 001 \rangle$  step segment. In effect, the former increases the attaching probability at the step segment aligned to  $\langle 110 \rangle$ , and the latter decreases the attaching probability at the step segment aligned to  $\langle 001 \rangle$ . With the edge diffusion being absent in our phase-field model, the effect of the diffusive anisotropy on the atomic attachment kinetic is mimicked by  $\tau(\theta)$ .

We write  $\tau(\theta) = \bar{\tau} [1 + \eta \cos(2\theta)]$  according to the twofold anisotropy of the atomic attachment kinetics. The parameter  $\tau(\theta)$  reaches the minimum at the island boundary that is along the  $x$  direction (where  $\theta = 90^\circ$  or  $270^\circ$ ) and the maximum at the island boundary that is along the  $y$  direction

(where  $\theta=0^\circ$  and  $360^\circ$ ). The minimum  $\tau_{\min}=\bar{\tau}[1-\eta]$  indicates the locally fastest attachment kinetics, while the maximum  $\tau_{\max}=\bar{\tau}[1+\eta]$  indicates the locally slowest attachment kinetics. Considering the high sticking probability at the  $\langle 110 \rangle$  step, we assume the instantaneous attachment kinetics limit for  $\tau_{\min}$ , which reduces to  $\tau_{\min}=a_1 a_2 W^3 / D d_0$ . Here, the  $x$  direction corresponds to  $\langle 110 \rangle$ , and the  $y$  direction  $\langle 100 \rangle$ . With  $\tau_{\min}$  fixed,  $\tau(\theta)$  is determined as  $\tau(\theta)=\tau_{\min}[1+\eta \cos(2\theta)]/(1-\eta)$  according to the local normal of the island boundary.

Equations (1) and (2), if the nucleation term and the random deposition term are absent, reduce to the BCF model of the step growth in thin interface limit  $W/x_s \rightarrow 0$ , where  $x_s$  is the diffusion length [16]. We have adopted the spatial varied diffusion  $D(\phi)$  and the orientation-dependent attachment kinetics  $\tau(\theta)$ . At this case, the phase-field model reduces to the BCF model with the step boundary condition modified according to the ES effect and the anisotropy. Therefore, when  $W$  is chosen far less than  $x_s$ , the phase-field simulated result is consistent with that of the BCF model. When the desorption is absent in our phase-field model, which indicates  $x_s = \infty$ , it is easy to meet the condition  $W \ll x_s$ .

Moreover, in order to reveal morphology of nucleation and growth of the islands, we need take into account another characteristic length, the island separation  $l_s$ . In the metal epitaxy  $l_s=(N_{\text{isl}}^{-1/2})$  reflects the island size (that determines the local radius of the compact island) and the island distribution at the nucleation regime, where  $N_{\text{isl}}$  is the island density [3]. The experimental values of  $l_s$  varies from tens to hundreds of  $a$  versus temperatures and fluxes [3]. For the simulation, we choose  $W=2a$ , which is reasonably smaller than  $l_s$  for the qualitative simulation. We take  $W$  as an input parameter, then determine  $\lambda$  and  $\tau$  according to Eqs. (3) and (4). In our simulation the thickness of STZ is  $3-6\Delta x$  with the grid spacing  $\Delta x=1a$  adopted, which presents enough resolution of the morphology of nucleation and growth of the islands.

### III. SIMULATED RESULTS

Referring the island growth on the W(110) surface [13,14], we adopt  $D=9000 \text{ \AA}^2/\text{s}$ , which corresponds to  $E_d=0.88 \text{ eV}$  with  $\nu=10^{12}$  at  $T=553 \text{ K}$ ,  $F=0.4 \text{ ML/s}$ ,  $E_s=0.125 \text{ eV}$ , and the nucleation parameter of  $\lambda_n=D$  and  $i=2$ . We estimate  $d_0=2.4 \times 10^{-3}$  for the qualitative simulations. The instantaneous attachment kinetics  $\beta_{\min}=0$  is assumed at the island boundary that is along the  $x$  direction. With  $\beta_{\min}=0$  is fixed, we use various anisotropy magnitudes  $\eta=0.3, 0.5, 0.6, 0.8, 0.9$ , and  $0.95$ , to describe increasingly limited attachment kinetics at the island boundary whose edge orientation deviates to the  $x$  direction.

The simulated images in Fig. 2 reveals formation and growth of the stripe arrays as the coverage increases when  $\eta=0.8$ . At the low coverage, there grow the high density of small islands, which are 3–4 ALs high, elongated in the  $y$  direction, and uniformly distributed, as shown in Fig. 2(a). For larger coverages, as shown in Figs. 2(b) and 2(c), new islands nucleate and grow on the upper ALs, while the base layers of the islands become connected and represent optional coalescence in the  $y$  direction, which forms stripes of

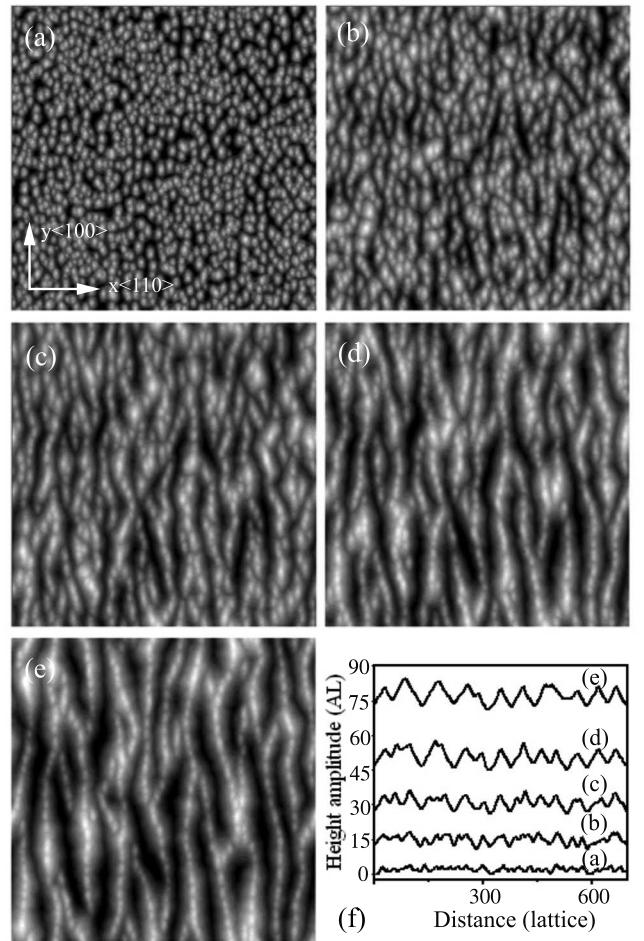


FIG. 2. The stripe morphology with the increasing coverages 2 ML (a), 15 ML (b), 30 ML (c), 50 ML (d), and 80 ML (e), simulated for the anisotropy magnitude  $\eta=0.8$ , and the corresponding cross-section profiles in (f). The simulated scale corresponds to  $210 \times 210 \text{ nm}^2$  of the W (110) surface.

islands. In Fig. 2(d) the stripes of islands become increasingly developed, as the stripe length (longitudinal length of one stripe keeping isolate before merging into the other) increases with the coverage. At the same time, coalescence of neighbor stripes causes the increasing period of stripes (transversal peak-peak distance of neighbor stripes). The height amplitude (peak-valley height difference) increases with time. Finally in Fig. 2(e) the periodical arrays of the stripes are achieved of sharply faceted slopes. The modulation of the period and the height amplitude versus the increasing coverages is further illustrated in Fig. 2(f).

The morphology of the stripe arrays is further adjusted by the anisotropy magnitude, as shown in Figs. 3(a)–3(e). In the limit of the large anisotropy magnitudes  $\eta=0.9$  and  $\eta=0.95$ , the stripe ridges become sharp and faceted and at the same time neighbor stripes occur significant coalescence at the valleys. The coalescence breaks the period of stripes, as illustrated by the irregular oscillation of the height amplitude in Fig. 3(f). In the other limit of  $\eta=0.3$ , the optional growth of the islands in the  $y$  direction becomes slow. With the bottom layers being connected for the stripe base, big mounding islands prevail on the upper ALs. Being interme-

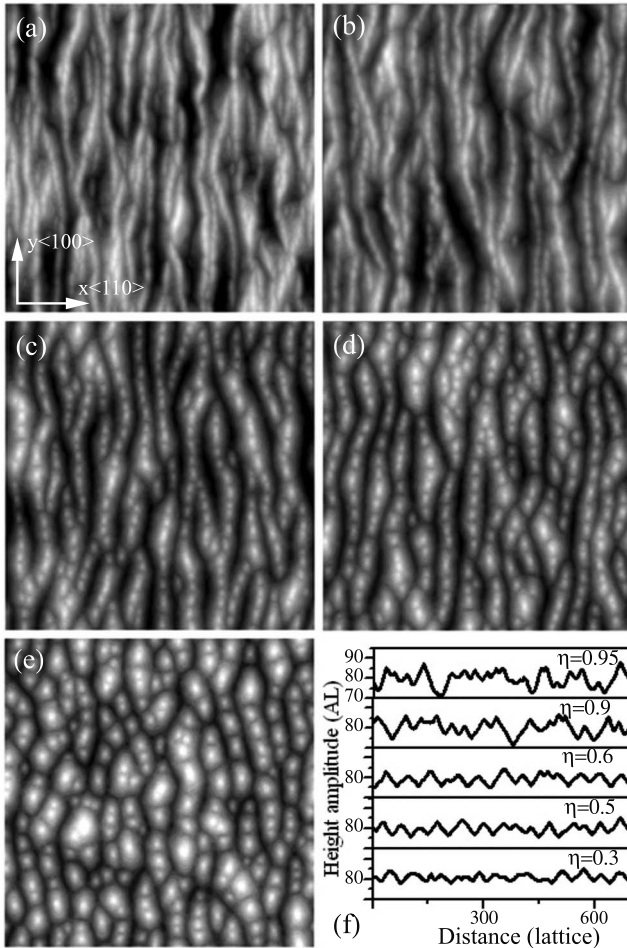


FIG. 3. The stripe morphology simulated for the different anisotropy magnitude of  $\eta=0.95$  (a), 0.9 (b), 0.6 (c), 0.5 (d), and 0.3 (e) with the coverage 80 ML and the corresponding cross-section profiles in (f). The simulated scale corresponds to  $210 \times 210 \text{ nm}^2$  of the W (110) surface.

diate between the two limits, the long stripes form at the cases of  $\eta=0.5$  and 0.6. The stripes are of continuous and gentle ridges, on which small islands form the local peaks, as denoted by light spots along the ridges. The cross-section profiles in Fig. 3(f) illustrate that the arrays of stripes simulated at the cases of  $\eta=0.5$  and 0.6 are of the reduced height amplitude, but with the regular period, as compared with that achieved for  $\eta=0.9$  and  $\eta=0.95$ . In the cases of  $\eta=0.5$  and 0.6, the stripe arrays evolve into the regular periodic structure of hills and grooves as the coverage increases further, as shown in Fig. 4, which resembles the reported morphology of the stripe arrays on the W(110) surface [13,14].

We analyze the height-height correlation of the simulated morphologies. First, the roughness  $w$  is calculated according to the root mean square of the local height  $\phi(\vec{r})$ . As illustrated in Fig. 5,  $w$  increases with the coverage  $\vartheta$ , indicating the kinetic roughening. The roughening rate  $m$  is measured by the power law index in  $w = \vartheta^m$ . In Fig. 5,  $m$  increases with  $\eta$ . In contrast to the weak kinetic roughening as described by  $m=0.26-0.31$  in the case of  $\eta=0.3-0.6$ , the strong roughening kinetics is indicated by  $m=0.35-0.68$  in the cases of  $\eta=0.8-0.95$ .

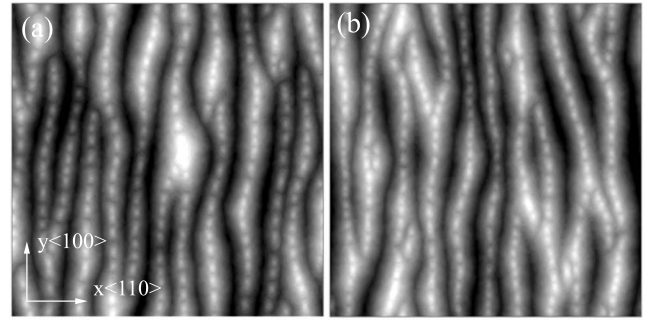


FIG. 4. The morphology of the regular stripe arrays simulated by using the anisotropy magnitudes of  $\eta=0.5$  (a) and  $\eta=0.6$  (b) with the coverage 200 ML. The simulated scale corresponds to  $210 \times 210 \text{ nm}^2$  of the W (110) surface.

Further, the height-height correlation function is calculated according to  $H_{\vec{v}}(l) = \frac{1}{S} \int d\vec{r} \phi(\vec{r}) \phi(\vec{r} + l\vec{v})$ , where  $S$  is the simulation domain area. With  $\vec{v}$  being  $\vec{y}$  and  $\vec{x}$ ,  $H_{\vec{v}}$  presents the correlation lengths,  $L_y$  in the  $y$  direction and  $L_x$  in the  $x$  direction. As shown in Fig. 6,  $L_y$  increases versus  $\vartheta$ , illustrating coarsening in the  $y$  direction. According to  $L \sim \vartheta^{n_y}$ ,  $L_y$  is fitted globally with  $n_y=0.49-0.68$  for  $\eta=0.3-0.95$ . Here,  $n_y$  increases with  $\eta$ , indicating enhancement of coarsening in the  $y$  direction versus the anisotropy magnitude. For the stripe growth, there are two characteristic lengths in the  $y$  direction, one is the stripe length, and the other is the size of the islands that nucleate and grow on the upper ALs. The upper-AL islands are of less geometric aspect ratio than the stripes at the base. As shown in Fig. 3, the upper-layer islands becomes more and more significant with the decreasing anisotropy magnitude. Therefore, during the global coarsening of the stripe length, temporary subscaling of  $L_y$  is also found in the case of the reduced  $\eta$ ,  $\eta=0.3-0.8$ , which becomes significant (denoted by the short fit line) at a later stage. The subscaling describes coarsening of the islands on the upper ALs.

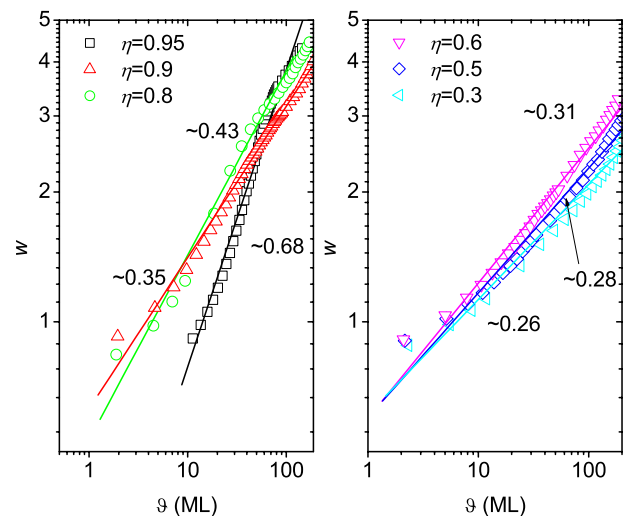


FIG. 5. (Color online) The evolution of the roughness  $w$  versus the coverage  $\vartheta$  of the stripe morphology simulated for the anisotropy magnitudes of  $\eta=0.3-0.95$ .

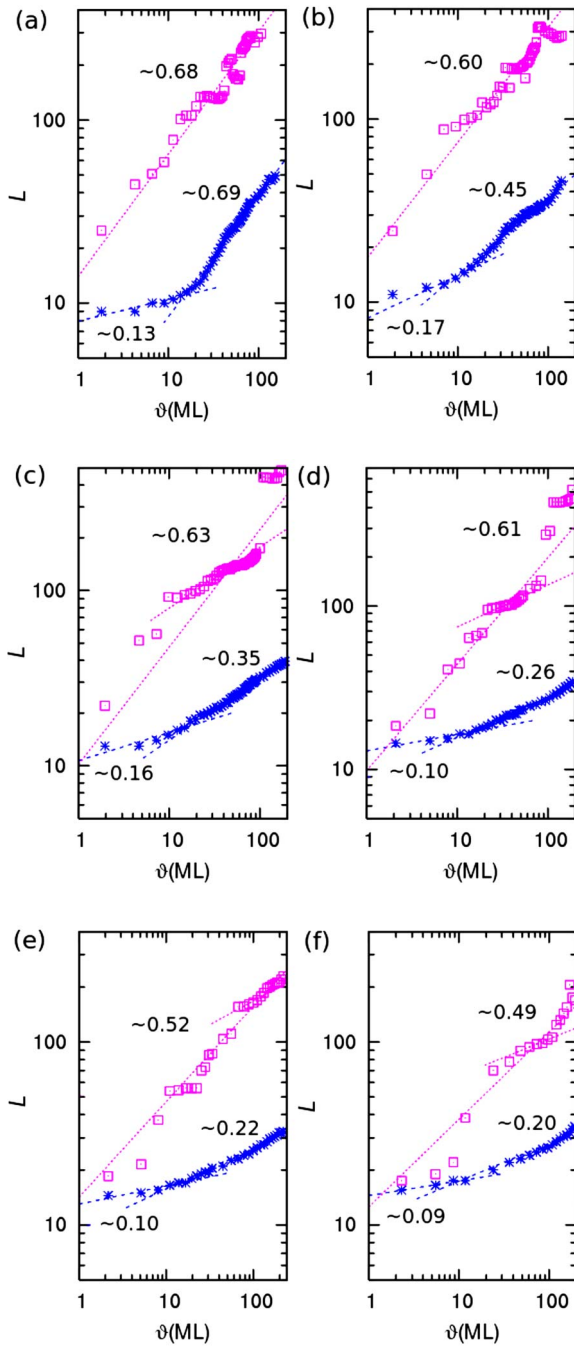


FIG. 6. (Color online) The evolution of the characteristic lengths  $L_x$  (cross) in the  $x$  direction and  $L_y$  (square) in the  $y$  direction, versus the coverage  $\vartheta$  during the stripe growth simulated for the different anisotropy magnitudes of  $\eta=0.95$  (a),  $\eta=0.9$  (b),  $\eta=0.8$  (c),  $\eta=0.6$  (d),  $\eta=0.5$  (e), and  $\eta=0.3$  (f). The jump in the characteristic length  $L_y$  above  $L=200$  in (c) and (d) is probably due to finite size effects.

The length  $L_x$  describes the period of the stripe arrays, whose coarsening is measured in terms of  $L \sim \vartheta^{n_x}$ . Initially,  $n_x$  is small of 0.09–0.17 for  $\eta=0.3$ –0.95, indicating the significant inhibition of coarsening in the  $x$  direction. With  $n_x \ll n_y$ , difference of the coarsening rates at the two directions explains the stripe formation at the early stage. At the subsequent stage,  $n_x$  turns to increase rapidly, approaching to the

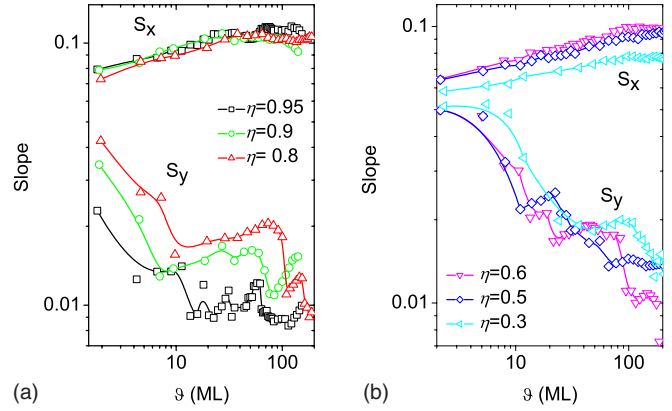


FIG. 7. (Color online) The evolution of the stripe slopes,  $S_x$  in the  $x$  direction and  $S_y$  in the  $y$  direction, versus the coverage  $\vartheta$  of the stripe morphology simulated for the anisotropy magnitudes of  $\eta=0.3$ –0.95.

roughening rate  $m$ . At the final stage  $n_x$  becomes steady with  $n_x=0.20$ –0.69 for  $\eta=0.3$ –0.95. At the cases of  $\eta=0.5$  and  $\eta=0.6$ ,  $n_x$  is small and difference of  $n_y$  and  $n_x$  remains large, which elucidates the persisting uniaxial growth of the slow transversal coarsening. In contrast, at the cases of  $\eta=0.9$  and  $\eta=0.95$ , difference of  $n_y$  and  $n_x$  decreases at the later stage, which indicates decay of the uniaxial growth trend in the  $y$  direction.

The stripe slopes are calculated by  $S_x=w/L_x$  and  $S_y=w/L_y$  along the  $x$  and  $y$  directions, respectively. In Fig. 7,  $S_x$  first increases with  $\vartheta$ , then turns to convergence that corresponds to the selected transversal slope of the stripe. At the same time,  $S_y$  decreases with  $\vartheta$ . In the case of  $\eta=0.9$  and  $\eta=0.95$ , the decrease of  $S_y$  becomes slow at the later stage. There exists the temporary plateau during  $S_y$  decreasing at the case of  $\eta=0.3$ –0.8, which corresponds to the subscaling of  $L_y$  with  $n_y \approx m$ .

#### IV. DISCUSSION

As the simulated results revealed, formation and growth of the stripe arrays is adjusted by the anisotropy magnitude of the atomic attachment kinetics. On the one hand, the anisotropic atomic attachment kinetics causes the different growth velocity in the  $x$  and  $y$  directions, which contributes to the anisotropic island shape and the different coarsening rates in the two directions. While coarsening in the  $x$  direction is suppressed, coarsening in the  $y$  direction is enhanced increasingly with the anisotropy magnitude. The difference of the coarsening rates in the two directions causes the stripe formation. On the other hand, the limited atomic attachment enhances the island roughening. Between the two possible actions of adatoms on the terraces, nucleation, or attachment at the exist steps, nucleation is increased when attachment at steps is limited. Under the ES barrier, increase of the island nucleation causes stronger roughening. The large anisotropy magnitude indicates that the atomic attachment kinetics is increasingly limited at the island boundary, despite of the instantaneous attachment kinetics at the segment that is along the  $x$  direction. The rapidly roughening kinetics is in-

trigued at the case of the large anisotropy magnitude, as evidenced by increasing of  $m$  versus  $\eta$ . Therefore, the large anisotropy magnitude causes not only the larger coarsening rate in the  $y$  direction, but also the stronger roughening kinetics.

At the long time scale, coarsening competes with roughening, as driven by minimization of the total step free energy of the stripes of islands. This competition is reflected by evolution of the slopes at the  $x$  and  $y$  directions. In the  $x$  direction,  $n_x$  turns to increase, approaching  $m$  at the later stage, so that a selected transversal slope is reached. In the  $y$  direction, owing to the anisotropy,  $n_y$  is larger than  $m$ , therefore, the stripes of islands grow with the decreasing longitudinal slope to represent the uniaxial growth along the  $y$  direction. For the upper-layer islands on the stripe ridge, the slope selection is expected in both  $x$  and  $y$  directions, hence the subscaling of  $n_x$  and  $n_y$  keeps temporarily consistent during approaching  $m$ . Therefore, starting with nucleation, growth, and coalescence of the anisotropic islands, the stripe arrays develop a quasiperiodic uniaxial structure with the selected transversal slope and the decreasing longitudinal slope by following  $m \sim n_x < n_y$  at long times.

The periodicity of the stripe arrays is determined by both coarsening rates in the  $x$  and  $y$  directions. For the isotropic pyramids and mounds, the typical coarsening rate is close to  $1/4$  as reported from experiments and simulations [1–3,24,25]. In our simulations for the stripe islands, the longitudinal coarsening rate is far larger than  $1/4$  in the  $y$  direction, enhanced by the anisotropy. However, in the other direction, the transversal coarsening rate changes with the roughening rate. When the kinetics roughening is fast, the transversal coarsening rate also becomes larger than  $1/4$ , which breaks the uniaxial growth of the stripe arrays and causes the irregular period, as simulated for  $\eta=0.9$  and  $\eta=0.95$ . At the case of the weak roughening, the transversal coarsening rate is slow, being close to  $1/4$ , which allows for the persistent uniaxial growth of the strip arrays of the increasing longitudinal length and the regular period, as revealed in the simulation of  $\eta=0.5$  and  $\eta=0.6$ . The stripe arrays of the regular period in our simulations have similar

scaling laws with the rectangular rippled state of  $m \sim n_x = 0.25$  and  $n_y = 0.5$  [9,26]. The scaling laws explain the growth of the stripe arrays as one intermediary state preceding to one-dimensional period state on (110) surfaces.

## V. CONCLUSION

Considering the anisotropic atomic attachment kinetics and the ES barrier, we simulate nucleation and growth of islands on the metal bcc (110) surfaces by using a phase-field model, which reproduces formation and growth of stripe arrays for various anisotropy magnitudes. The atomic attachment kinetics is locally limited at the island boundary that is along the  $y$  direction, whereas instantaneous atomic attachment kinetics is assumed at the island boundary that is along the  $x$  direction. While coarsening is fast in the  $y$  direction, coarsening becomes slow in the  $x$  direction at the early stage, owing to the anisotropy, which leads to formation of the stripe arrays. The stripe arrays assemble a quasiperiodic uniaxial structure of the selected transversal slope and the decreasing longitudinal slope by following  $m \sim n_x < n_y$  at the long time scale. At the case of the large anisotropy, rapid roughening is induced by the strongly limited attachment kinetics, and then  $n_x$  becomes large, which breaks the uniaxial growth finally. In the regime of the weak roughening at the case of the reduced anisotropy magnitude, large  $n_y$  is achieved with  $n_x \sim m$  remaining slow, which contributes to the stripe arrays of the regular period and the increasing uniaxial length.

## ACKNOWLEDGMENTS

This work has been partially supported by EU FP6, through NMP STRP Grant No. 016447 “MagDot,” by the Chinese Department of Science and Technology under the National Basic Research Program (Grant No. 2005CB623602), by the Natural Science Foundation of China (Grant Nos. 10774180 and 60621091), and by the Chinese Academy of Sciences (Grant No. KJCX2.YW.W09-5).

- 
- [1] P. Politi, G. Grenet, A. Marty, A. Ponchet, and J. Villain, *Phys. Rep.* **324**, 271 (2000).
  - [2] T. Michely and J. Krug, *Islands, Mounds, and Atoms* (Springer, Berlin, 2004).
  - [3] J. W. Evans, P. A. Thiel, and M. C. Bartelt, *Surf. Sci. Rep.* **61**, 1 (2006).
  - [4] R. L. Schwoebel, *J. Appl. Phys.* **40**, 614 (1969).
  - [5] J. Villain, *J. Phys. I* **1**, 19 (1991).
  - [6] A. Pimpinelli, I. Elkinani, A. Karma, C. Misbah, and J. Villain, *J. Phys.: Condens. Matter* **6**, 2661 (1994).
  - [7] A. Pimpinelli, V. Tonchev, A. Videcoq, and M. Vladimirova, *Phys. Rev. Lett.* **88**, 206103 (2002).
  - [8] F. Hontinfinde, and R. Ferrando, *Phys. Rev. B* **63**, 121403(R) (2001).
  - [9] L. Golubović, A. Levandovsky, and D. Moldovan, *Phys. Rev. Lett.* **89**, 266104 (2002).
  - [10] M. Albrecht, H. Fritzsche, and U. Gradmann, *Surf. Sci.* **294**, 1 (1993).
  - [11] U. Köhler, C. Jensen, A. C. Schindler, L. Brendel, and D. E. Wolf, *Philos. Mag. B* **80**, 283 (2000).
  - [12] U. Köhler, C. Jensen, C. Wolf, A. C. Schindler, L. Brendel, and D. E. Wolf, *Surf. Sci.* **454–456**, 676 (2000).
  - [13] B. Borca, O. Fruchart, F. Cheynis, M. Hasegawa, and C. Meyer, *Surf. Sci.* **601**, 4358 (2007).
  - [14] B. Borca, O. Fruchart, Ph. David, A. Rousseau, and C. Meyer, *Appl. Phys. Lett.* **90**, 142507 (2007).
  - [15] F. Liu and H. Metiu, *Phys. Rev. E* **49**, 2601 (1994).
  - [16] A. Karma and M. Plapp, *Phys. Rev. Lett.* **81**, 4444 (1998).
  - [17] F. Otto, P. Penzler, A. Rätz, T. Rump, and A. Voigt, *Nonlinearity* **17**, 477 (2004).

- [18] A. Rätz and A. Voigt, *J. Cryst. Growth* **266**, 278 (2004).
- [19] A. Rätz, A. Ribalta, and A. Voigt, *J. Comput. Phys.* **214**, 187 (2006).
- [20] Y. M. Yu and B. G. Liu, *Phys. Rev. B* **70**, 205414 (2004).
- [21] Y. M. Yu and B. G. Liu, *Phys. Rev. E* **69**, 021601 (2004).
- [22] J. W. Evans and M. C. Bartelt, *J. Vac. Sci. Technol. A* **12**, 1800 (1994).
- [23] A. Karma and W. J. Rappel, *Phys. Rev. E* **57**, 4323 (1998).
- [24] P. Šmilauer and D. D. Vvedensky, *Phys. Rev. B* **52**, 14263 (1995).
- [25] D. Moldovan and L. Golubovic, *Phys. Rev. E* **61**, 6190 (2000).
- [26] A. Levandovsky and L. Golubović, and D. Moldovan, *Phys. Rev. E* **74**, 061601 (2006).